Unraveling LIS1-Lissencephaly: Insights from Cerebral Organoids Suggest Severity- Dependent Genotype-Phenotype Correlations, Molecular Mechanisms and Therapeutic Strategies

Lea Zillich, Andrea Carlo Rossetti, Olivia Fechtner, Matteo Gasparotto, Camille Maillard, Anne Hoffrichter, Eric Zillich, Ammar Jabali, Fabio Marsoner, Ruven Wilkens, et al.

Unraveling LIS1-Lissencephaly: Insights from Cerebral Organoids Suggest Severity-Dependent Genotype-Phenotype Correlations, Molecular Mechanisms and Therapeutic Strategies

Lea Zillich[1,2,3,4,+], Andrea Carlo Rossetti[1,2,3,+], Olivia Fechtner[1,2,3,5,+], Matteo Gasparotto[1,2,3], Camille Maillard[6], Anne Hoffrichter[1,2,3], Eric Zillich[5], Ammar Jabali[1,2,3], Fabio Marsoner[1,2,3], Ruven Wilkens[1,2,3], Christina B. Schroeter[7], Andreas Hentschel[8], Sven G. Meuth[7], Tobias Ruck[7], Philipp Koch[1,2,3], Andreas Roos[7,9], Nadia Bahi-Buisson[6], Fiona Francis[10,11,12], Julia Ladewig[1,2,3*]

[1]Department of Translational Brain Research, Central Institute of Mental Health, Medical Faculty Mannheim, Heidelberg University, Mannheim, Germany. [2]HITBR Hector Institute for Translational Brain Research gGmbH, Mannheim, Germany. [3]German Cancer Research Center (DKFZ), Heidelberg, Germany. [4]Department of Genetic Epidemiology in Psychiatry, Central Institute of Mental Health, Medical Faculty Mannheim, Heidelberg University, Mannheim, Germany. [5]Institute of Reconstructive Neurobiology, University of Bonn School of Medicine & University Hospital Bonn, Bonn, Germany. [6]Department of Pediatric Neurology, Université Paris Descartes, Imagine Institute, Paris, France. [7]Department of Neurology, Medical Faculty and University Hospital Düsseldorf, Heinrich Heine University Düsseldorf, 40225 Düsseldorf, Germany, [8]Leibniz-Institut für Analytische Wissenschaften - ISAS, Dortmund, Germany, [9]Division of Neuropediatrics, Center for Translational Neuro- and Behavioral Sciences (C-TNBS), University Hospital Essen, Germany, [10]INSERM UMR-S 1270, F-75005 Paris, France. [11]Sorbonne University, F-75005 Paris, France. [12]Institut du Fer à Moulin, F-75005 Paris, France.

[+] These authors equally contributed to this work.

[*] Corresponding author

Correspondence: Julia.Ladewig@zi-mannheim.de

Abstract

Lissencephaly is a developmental cortical malformation characterized by reduced to absent gyri and a disorganized cortex, often leading to severe impairments in affected individuals and a reduced life expectancy. Heterozygous mutations in the *LIS1* gene, encoding a regulator of the microtubule motor dynein, cause lissencephaly with different clinical severities. While the clinical disease spectrum correlates with the degree of lissencephaly, location and type of mutation may not. We leveraged forebrain-type organoids from LIS1-lissencephaly patients, diagnosed with mild, moderate or severe lissencephaly to investigate, in a cytoarchitecture and multi-omics approach, how the severity degree in patients might relate to specific mutations in the *LIS1* gene. We questioned which processes during cortical development might be differentially affected by severity grade, and whether they could be pharmacologically targeted. We found alterations in neurodevelopment often with a severity-dependent gradient. Specifically, we identified alterations of the cytoarchitecture, progenitor cell homeostasis and neurogenesis. Particularly important disease-linked molecular mechanisms were microtubule destabilization, WNT-signaling, and perturbed cadherin- and unfolded protein-binding. Some mechanisms exhibited a severity-dependent gradient, or were specific to a severe grade. We present strategies to reverse phenotypic changes in LIS1-patient organoids, and an *in silico* approach with therapeutic potential. Thus, we show that different LIS1-severity grades can be recapitulated *in vitro*, that there is a direct link between the phenotype and genotype, that organoid-based disease modeling can identify molecular underpinnings of malformations of cortical development and that organoids provide a valid platform to develop and test therapeutic strategies.

Keywords

LIS1, lissencephaly, forebrain organoids, neural progenitors, scRNA-seq, proteomics, neurodevelopment, disease modeling

Introduction

The human neocortex, critical for language, sociability and sensorimotor control, is an expanded, highly organized and extensively folded –gyrencephalic- structure (1). Although current understanding of how the human cortex develops has been obtained through the study of model systems, the applied models often involve species with a smooth (lissencephalic) brain surface, such as mice. Thus, key cellular events that impact human-specific brain expansion and our understanding of how disease-linked mutations disrupt human cortical development remain elusive. Malformations of human cortical development are a vast and heterogeneous group of disorders with genetic or environmental aetiology, and are characterized by disruption of cerebral cortex architecture (2). Heterozygous mutations in the *LIS1* gene cause lissencephaly (smooth brain; MIM: 607432) in humans with diverse neuroimaging phenotypes, ranging from mild pachygyria (broad gyri) to severe agyria (no gyri), resulting in clinical phenotypes including epilepsy and intellectual disabilities (3). So far, treatment options for LIS1-lissencephaly are limited and affected individuals often experience severe symptoms throughout a significantly shortened lifespan (4, 5). While the clinical severity generally correlates with the degree of lissencephaly, the location and type of the underlying *LIS1*-mutation may not, in turn making genotype-phenotype correlations challenging (6). Studies of *Lis1* mouse models unveiled a role of the Lis1 protein in the regulation of microtubule motor cytoplasmic dynein, and through this function, dynein-dependent processes such as neuronal migration, interkinetic nuclear migration and mitotic spindle orientation in progenitor cells (7-10). Although the phenotypes observed were dramatically milder in mouse models - which are inherently lissencephalic - than in humans, these studies suggested that Lis1 protein dosage may be relevant to phenotypic severity (11, 12). However, no study has yet established a clear correlation between the clinical phenotype, neuroimaging data and patient-specific *LIS1*-mutations in terms of a robust genotype-phenotype correlation. Thus, the questions, (I) how LIS1-lissenencephaly severity grades can be modeled *in* vitro and related to specific mutations in the *LIS1* gene, (II) whether specific processes during cortical development are differentially affected by severity grades, and (III) if processes linked to LIS1-lissencephaly can be reversed or reduced through pharmacological treatments, remain unaddressed.

Due to the limited access to human postmortem brain tissue from LIS1-lissencephaly patients (LIS1-patients) at different developmental stages, it is difficult to study disease- and severity-related molecular and cellular drivers in the human context. By applying

instructive signals to aggregated human induced pluripotent stem (iPS) cells, self-organizing cerebral organoids resembling specific brain regions including the dorsal forebrain can be generated (13). Forebrain-type organoids develop a ventricular zone (VZ), a subventricular zone and a cortical plate-like structure in which neurons from different cortical layers can be identified in a spatially organized manner. Comparative transcriptional profiling of cerebral organoids with human primary brain tissue has demonstrated a remarkable overlap, in both, bulk tissues and at the single-cell level (14, 15). Thus, human brain organoids represent an experimental model that most closely mimics early human brain development at cellular and transcriptional levels. Although we and others previously demonstrated that cerebral organoids represent a valid experimental tool to model the most severe form of LIS1-lissencephaly, Miller-Dieker syndrome (MDS, MIM: 247200) (16, 17), there has not been a model of different LIS1-lissencephaly severity grades to study the impact on clinical phenotypes *in vitro*, so far. In MDS patient-derived human cerebral forebrain-type organoids, we observed that LIS1 deficiency results in an impairment of ventricular niche signaling and cell fate control via the N-cadherin/ß-catenin signaling axis (16). However, as a contiguous gene deletion syndrome, MDS does not only involve *LIS1*.

Here, we applied reproducible patient-specific forebrain-type organoids and cortical progenitors to investigate the role of six human *LIS1*-mutations and their association with the different disease severities of LIS1-lissencephaly. We report a gradient of phenotypic changes, including alterations in cytoarchitecture, progenitor cell homeostasis and neurogenesis. We show that the degree of alteration can be aligned with the clinical severity grade of LIS1-lissencephaly, but is homogeneous within one severity grade, independent of specific *LIS1*-mutations. In a single-cell analysis, we show for the first time, a *LIS1*-mutation severity-dependent dysregulation of progenitor cell homeostasis affecting neuroepithelial (NE) and radial glial (RG) cells. We show in -omics analyses that these changes are likely caused through increased neurogenesis and are associated with the degree of microtubule destabilization, N-cadherin binding, and alterations in niche-dependent WNT signaling, which we then validated using molecular biology methods. Furthermore, our proteomics data identified a decrease in the absolute LIS1 amount with increasing severity grade, and showed that this is accompanied by a severity grade-specific mis-regulation of translational activity and an increase in proteasomal and signalosomal proteins. We provide proof of principle for *in vitro* drug testing to reverse molecular

phenotypes associated with LIS1 severity grade and *in silico* drug repurposing to identify future targets, hence, proving our model to be suitable for future drug screening analyses.

Thus, our work (i) provides a proof of principle that carefully calibrated forebrain-type organoids represent a homogeneous and fine-tuned system that captures different severity grades of a cortical malformation across different genetic backgrounds and (ii) along this line enables significant insights into the molecular etiology of phenotypical manifestation and (iii) also provides a platform to perform drug screenings. Hence, this may allow the identification of novel disease mechanisms even appearing at very early stages of development and the development of therapeutic strategies.

Results

Premature neurogenesis and perturbed progenitor cell homeostasis in *LIS1*-patient derived cerebral organoids.

From a cohort comprising 63 cases, we selected seven LIS1-patients covering the whole spectrum of gyrification alterations of LIS1-lissencephaly, ranging from Dobyns grade 5 (mild) to 1 (severe) (18, 19) (for more details on MRI data see Philbert, Maillard (20) and Sup. Fig. S1A-B; for selection criteria see Material and Methods section). Each patient harbors a molecularly characterized heterozygous pathogenic variant in the *LIS1* gene (Sup. Fig. S1B). Following reprogramming of patient-derived somatic cells to iPS cells, and their basic characterization (2 clones each, Supplementary Fig. 1C-J, Sup. Table S1), we validated the respective patient-specific *LIS1* mutations by sequencing (Sup. Fig. 1K-M). We then generated forebrain-type cerebral organoids (13) from the seven LIS1-patients and seven control iPS cell lines. While organoids from controls and patients with a milder malformation gradually developed regular neuroepithelial loop-like structures, organoids from patients with a moderate disease grade appeared generally smaller in size (Fig. 1A; Sup. Fig. S2A). Organoids from severely affected patients were not smaller compared to control-derived organoids but developed irregular edges, with single cells noticeably growing out from the structures (Fig. 1A; Sup. Fig. 2A). Immunohistochemical analyses following whole-tissue clearing or cryo-sectioning showed that all successfully generated organoids from severe malformation patients present a large belt of neurons which was less abundant in mild and moderate conditions and nearly absent in control-derived organoids at this age (Fig. 1B, Sup. Fig. S2A-B). When we further assessed the architecture of the individual VZ-like structures within the organoids by analyzing multiple VZ-like morphological parameters, i.e. the apical and basal membrane lengths, the diameter, and VZ and total loop areas (16), we identified a

significant reduction of all variables in organoids derived from patients with moderate and severe diagnosis, as well as a significant reduction in three out of the six parameters analyzed in organoids from patients with mild grade LIS1-lissencephaly compared to controls (Fig. 1C-D, Sup. Fig. S2C-G, Sup. Table S2). When investigating disease severity-specific changes in cellular composition in more complex stratified organoids, we identified an increase in the abundance of cells expressing basal radial glia (bRG) markers with increasing severity, accompanied by a decrease in deep cortical layers and a gradual increase in markers specific to upper cortical layer neurons. (Fig. 1E-G). Taken together, our morphological characterization suggests severity-dependent alterations of progenitor cell homeostasis and neurogenesis.

Multi-omics analyses suggest shared and severity-specific molecular alterations underlying the phenotypic changes across the different LIS1-severity grades.

To further investigate the underlying molecular mechanisms of the severity-dependent gradient in phenotypic changes, we profiled early-stage organoids by single-cell RNA sequencing (scRNA-seq; two to three pooled organoids at day 23±2 from two different genotypes per condition; Fig. 2A, Sup. Fig. S3A-B). Here, we observed high homogeneity in cell type composition for each severity grade, across the patient-specific genetic backgrounds (Sup. Fig. 3A). We identified nine cell populations based on known marker genes including neuroepithelial cells (NE), cycling progenitors (CyP), radial glia cells (RG), intermediate progenitors (IP), dorsal forebrain (dFB-N), ventral forebrain (vFB-N), midbrain (MB-N) and inter-neurons (IN), as well as astroglia cells (G) (21-25) (Sup. Fig. S3C). We further identified a progenitor cell cluster which exhibits a very similar marker profile as the RG population but clusters separately. GO term analyses revealed that this cell cluster distinguishes from the RG cluster by a significant overrepresentation of GO terms linked to neuronal differentiation, including generation of neurons, neuron fate commitment and regulation of neuron differentiation, thus termed transitory RG (t-RG; Fig. 2C-D, Sup. Fig. S3C, Sup. Table S3). A comparison of cell type composition between the severity grades revealed a significant reduction in neural progenitor cells accompanied by a significant increase of differentiated cells in the LIS1 severe grade condition, a cytological change that was less pronounced in mild and moderate conditions (Sup. Fig. S3D). When investigating the progenitor cell type composition in more detail (Fig. 2C; Sup. Fig. S3D), we identified a depletion of neuroepithelial (NE) cells in all patient samples. While the mild and moderate grade LIS1-patient organoids showed a relative increase in RG, the samples derived from

severe grade patients showed a significant depletion of this population, accompanied by a trend towards decreases in CyP and the appearance of the severe grade-specific t-RG cluster.

Differential RNA expression in progenitor cells.

To further elucidate common disease mechanisms and associated severity-dependent changes, we performed differential expression analysis in the pooled progenitor cell types (NE, RG, t-RG), excluding cycling progenitors to avoid confounding by cell cycle. This revealed 140 significantly differentially expressed genes in the mild, 80 in the moderate and 104 in the severe condition compared to the control condition (Figure 2E, Sup. Table S4-S6.), with shared and specific genes for each severity grade (Sup. Fig. 3E). In the mild condition, the most significant unique association was an upregulation of *FZD5*, encoding a receptor for the Wnt5A ligand involved in forebrain and cortical hem development (26). The long non coding RNA 51 found to be expressed in the human neocortex (27) and the proneurogenic gene *MEIS2*, a gene already associated with malformations of human cortical development (MCD) (25) were found to be the most significant uniquely associated genes with the moderate condition. In the severe condition, the top associations were a downregulation in *MTRNR2L12*, a gene associated with MCD and synaptic connectivity (28, 29) and an upregulation in *NNAT*, a gene involved in brain development (30). Several genes were differentially expressed across conditions, such as *DLK1*, a transmembrane protein regulating cell growth, and involved in neuronal differentiation and homeostasis (31), *SFRP1*, a WNT pathway modulator (32) and *LHX2* and *FOXG1*, both of which playing a fundamental role in early cortical specification (33, 34).

Differential protein expression and network analysis in progenitor cells.

To further investigate the common and severity-dependent pathomechanisms of LIS1-lissencephaly, we set out to elucidate the role of the different mutations in the *LIS1* gene in progenitor cells at the protein level. To this end, we generated homogeneous cortical progenitor cells according to established protocols (16, 35) (four to six samples per condition from two different genotypes) and quantified protein abundances using label-free mass spectrometry (Fig 2A). When comparing the proteomic signatures of the severity grades to the control condition, we observed 71 differentially regulated proteins in the mild, 93 in the moderate, and 335 in the severe grade patient-derived samples, although at nominal significance (Sup. Fig 3F, Sup. Table S7). Interestingly, we found that LIS1 protein levels were strongly decreased with a significant severity-grade dependent downregulation in

progenitor cells, whereas at the transcript level the strongest downregulation of LIS1 was observed in the mild severity grade. We further investigated RNA expression and protein levels of LIS1 interaction partners and identified severity-grade dependent significant changes in several LIS1 interaction partners, e.g. FUS, SRSF1, GSP90, SSB, DYNC1H1, and TUBB, with partly corresponding transcript levels (Fig. 3F). We further performed a network analysis (WGCNA) of the protein data and identified five modules, two of them significantly associated with the LIS1-lissencephaly severity grades (Fig. 3G). The turquoise module showed significant downregulation in the moderate and severe samples and GO enrichment analysis showed hereby, the inclusion of proteins involved in proteasomal protein degradation, ubiquitin-dependent protein catabolism, protein neddylation, cytoplasmic translation, and L-serine biosynthetic process (Sup. Figure S3G). Notably, several proteins involved in protein catabolism, including members of the proteasome and the COP9 signalosome, are found in this module, indicating that upregulation of protein catabolism is a feature shared by all LIS1-patient-derived organoids, regardless of the severity grade. In addition, the blue module showed an increasing severity grade-dependent negative correlation. GO enrichment analyses revealed that proteins belonging to this module were enriched amongst others for pathways related to RNA splicing, cadherin binding, G protein activity, and unfolded protein binding (Sup. Table S8). Network analysis of this module identified three major clusters (Figure 2H). Notably, the first subset of proteins includes such involved in RNA splicing that have been previously identified as nuclear interactors of LIS1 in *AGO2* gene knockout embryonic stem cells (36). Among them, NCL and DXCX3 have also been associated with pre-rRNA transcription, ribosome assembly, and translation of components of the core translational machinery (37, 38). The second and third groups contain proteins involved in ribosome assembly and enhancers of protein translation and proteins involved in endoplasmic reticulum (ER) protein folding, including the ER chaperone BiP, indicating that the mis-regulation of translational activity already suggested by components of the turquoise module may worsen in a severity-dependent fashion. We then confirmed the severity-dependent expression of selected proteins involved in unfolded protein binding and ER protein folding by immunofluorescence in LIS1 patient-derived forebrain organoids (Sup. Figure S3H).

Integrative Analysis of differential RNA and protein regulation.

We then performed an integrative GO enrichment analysis based on the results of the differential RNA and protein expression analyses for biological processes (Fig. 2J, full results

Sup. Table S9) and molecular functions (Sup. Fig. S3J, full results Sup. Table S10). Here, we found changes in a GO cluster connected to early brain development including forebrain development, neural precursor cell proliferation and regulation of neurogenesis, indicating early neurodevelopmental abnormalities in line with our morphological characterization of the patient-derived organoids. Interestingly, this cluster showed strong enrichment for differentially expressed genes across all severity grades, often with a severity-dependent gradient, at the RNA level and in the moderate and severe condition at the protein level. We also observed clusters with strong enrichment across all severity grades and -omics layers; one related to triphosphate metabolic processes and one related to RNA splicing and cytoplasmic translation, indicating broad changes in LIS1-lissencephaly independent of severity grade. For molecular functions, we showed beside others, enrichment for pathways related to tubulin-, actin-, cadherin-, and WNT-protein binding.

Perturbance in microtubule stability, N-cadherin scaffold-organization and WNT-signaling are critical severity grade-dependent phenotypes in LIS1-patient-derived organoids.

We investigated the GO term enrichment described above in more detail and identified amongst others a gradual deregulation of actin binding, actin filament binding and structural constitution of the cytoskeleton at the protein level with increasing severity grade. Moreover, these analyses revealed changes in the GO term referring to tubulin-binding (Fig 3A). To further investigate changes in the cytoskeleton in LIS1-patient-derived organoids; we performed immunostainings for acetylated (stable) alpha-tubulin (Ac-TUB). In whole-tissue cleared organoids we identified a clear overall reduction of Ac-TUB positive labeled structures, a cellular phenotype increasing with malformation severity compared to control samples (Fig. 3B). To quantify these changes in Ac-TUB, we investigated individual VZ structures in organoid cryosections. Here, we detected that in control conditions, the span of Ac-TUB strands was in close proximity and aligned from the apical to the basal side, while in patient-derived organoids, strand density was progressively decreased at the basal side with increased malformation severity (Fig. 3B-C, Sup. Table S11). Further, we investigated cadherin binding by measuring the accumulation of N-cadherin at the apical membrane alignment in LIS1-patient-derived organoids, which was also implicated in the GO analyses of differential RNA and protein expression (Fig. 3F, Sup. Fig. 3H). Doing so, we identified a disruption in all patient organoids, most significantly in the moderate and severe malformation conditions (Fig. 3D-F, Sup. Table S11).

The GO term enrichment analyses, our findings in an organoid based model for MDS (16), as well as a recent preprint applying an interdisciplinary approach including cerebral organoids to study LIS1-lissencephaly (39), suggest WNT signaling as a potential underlying patho-mechanism in LIS1-lissencephaly. Hence, we investigated WNT signaling in more detail. To monitor the onset and localization of WNT target gene activity in patient- and control-derived organoids, we developed WNT-GFP iPS cell reporter lines and differentiated them into forebrain-type organoids. We observed that the apical barrier of VZ structures from mild, moderate and severe grade LIS1-lissencephaly patients exhibit - with increasing disease severity - a gradual decrease of WNT-target reporter activity signal compared to control (Fig. 3G-H). Changes in WNT signaling can lead to a switch of apical RG cell division from progenitor cell expansion to neurogenesis (16). Therefore, we explored the expression of genes involved in WNT signaling in CyP – the population which is most likely to be associated with the progenitors at the apical surface – and found a major dysregulation particularly in the severe form of LIS1-lissencephaly (Fig. 3L). Consequently, we then analyzed the plane of cell division of cycling progenitors at the apical surface of control, mild, moderate and severe grade patient-derived organoids (Fig. 3J). Indeed, we identified a clear increase in horizontal division patterns of apical RG cells in cultures derived from severe grade patients compared to controls. In addition, we observed an increase in oblique division mode (most likely a direct effect of the perturbed microtubule array) in all patient samples, which appeared most prominently in patients with moderate- and severe-grade LIS1-lissencephaly (Fig. 3K).

Probing therapeutic targets in LIS1 patient-derived organoids

To identify possible rescue strategies for the alterations in cytoarchitecture and WNT-signaling in LIS1-patient-derived organoids, we investigated the effect of the FDA-approved drug EpothiloneD (a macrolide directly interacting with and stabilizing microtubules) (40-42) and of the GSK3ß inhibitor CHIR99021 (a WNT pathway modulator) (43) in LIS1-patient- and control-derived organoids. We confirmed that EpothiloneD treatment significantly increased the Ac-TUB strand density in basal VZ regions of LIS1-patient-derived samples (Fig. 4A, Sup. Table S13). We further detected that microtubule-stabilization significantly increased the thickness of VZ areas in organoids from LIS1 severe grade patients (Fig. 4B) and improved the organization of the apical membrane alignment (Fig. 4D-E, Sup. Tables S14-S15). In addition, the treatment resulted in a marked decrease of the neuronal belt surrounding the VZ structures, with the most obvious effect in organoids from patients with

moderate and severe grades (Fig. 4C). In the severe condition, we observed improvement of all VZ parameters (Sup. Fig. S4B, Sup. Table S14). Of note, our results are very homogeneous across different genetic backgrounds within the same severity grade. These data suggest that microtubule destabilization is not only a shared mechanism of LIS1-lissencephaly (16), but is also critical for developing the phenotype with a severity-dependent gradient and may represent a promising therapeutic target. When exposing LIS1-patient- and control-derived organoids to CHIR99021, we observed a more homogeneous generation of VZ structures, an increase in VZ thickness and a reduced neuronal belt surrounding the VZ area, most evident in severe grade patient-derived organoids (Fig. 4F-G, Sup. Fig. S4C, Sup. Table S14). In addition, the treatment rescues the switch in plane of cell division in organoids derived from severe grade patients while it does not significantly impact the plane of cell division in the control, mild and moderate conditions (Fig. 4H, Sup. Table S16). These data suggest that dysregulation of niche-dependent WNT-signaling strongly correlates with the most severe form of LIS1-lissencephaly and that the random change in division modes in the mild and moderate form of LIS1-lissencephaly most likely mirror the direct impact of the *LIS1* mutation on the microtubule array. At the same time, both CHIR and EpoD are difficult to apply in clinical settings, as they both have broad-range off-target effects that are not fully characterized yet (44). Therefore, we sought to identify possible additional rescue strategies for LIS1-lissencephaly, using a drug repurposing analysis in the RG cluster with CMap. The most significant negative connectivity score corresponding to the strongest potential of rescuing the LIS1-lissencephaly associated transcriptional alterations was observed for everolimus, an FDA-approved drug that has been implicated in other neurodevelopmental disorders characterized by cortical malformations (45, 46), validating the predictive power of this approach (Sup. Fig. S4D). For this mTOR inhibitor, we observed a severity-dependent increase in negative connectivity scores suggesting it as a potential pharmaceutical drug for different LIS1 phenotype severities. Results for the mode of action category in CMap further support inhibitors of mTOR and its upstream regulator PI3K as candidate drugs to rescue the LIS1 phenotype (Sup. Fig. S4D).

Discussion

By combining a cytoarchitecture and multi-omics approach for LIS1-severity-grade dependent forebrain organoid models, we identified LIS1-lissencephaly associated pathological changes as well as novel common and severity-specific underlying mechanisms. Our data show that different patient-specific mutations in the *LIS1* gene have convergent

cellular and molecular impacts on the *in vitro* phenotype, for which we can associate severity with the neuroimaging diagnosis of the patient. Thus, our study provides a strong correlation between the patient-specific genetic background - including the respective mutation in the *LIS1* gene - and the clinical severity grade and highlights the potential role of different degrees of neural progenitor perturbation in the manifestation of the disease. Further our -omics results are consistent with the hypothesis that degradation of mutant LIS1, suggested by the decrease in the absolute LIS1 amount and by the increase in proteasomal and signalosomal proteins, might affect cell homeostasis in two different ways. Firstly, the reduced amount of functional LIS1 results in a deregulation of cytoarchitecture. Secondly, mis-regulation of LIS1 nuclear partners, associated with the increase in pro-translational factors, may result in aberrant protein translation, and increase in ER stress.

Cytoskeletal destabilization represents a major pathophysiological hallmark impacting the severity grade-dependent phenotype in LIS1-patient-derived organoids. Our assays indicate a strong upregulation of TUBB, and downregulation of TUBG1 and several members of the dynein complex, besides a disorganization of the acetylated tubulin network. The microtubule network has been found to be associated with proper membrane transport and recycling of N-cadherin (47), whose signaling was found to be altered by our -omics data. Alteration of the N-cadherin-based adherens junction scaffold might interfere with the maintenance of the proliferation, differentiation, and stemness properties of the NE and RG cells in the early phases of cortical development (48, 49), and could partially explain the increased neurogenesis we observed in severe grade organoids. Coherent with this, a higher degree of disruption of the N-cadherin scaffold at the apical membrane could have detrimental effects on beta catenin-mediated WNT signaling (16, 50) and as such, on the neurogenic transition of the RG pool, and - in parallel - an increased neurogenesis, as observed in the severe grade patient-derived organoids. Indeed, the WNT pathway has been demonstrated to be crucial in regulating neurogenesis and progenitor survival (51). Notably, we unveiled – to our knowledge for the first time - that a common mechanism across all severity grades of LIS1-lissencephaly is the depletion of NE cells, one of the most sensitive progenitor populations in the developing cortex, related to alterations of spindle orientation during mitosis (9, 52). We also describe a significant increase in RG cells in LIS1-patient-derived organoids. These data point towards a disease-specific premature conversion of NE cells into the later stem cell stage of RG cells. Further, a significant proportion of t-RG-cells in severe grade patient-derived organoids as well as the appearance of cells expressing bRG markers with increased severity grade in more complex organoid cultures supports the identified gradual impairment

of progenitor homeostasis and increased premature neurogenesis from mild, moderate to severe patient-derived organoids. Of note, the proliferative capacity and the neurogenic potential of NE and RG cells are among the cardinal pillars of the expansion and development of the human neocortex (1, 53, 54).

Perturbed cytoskeletal arrangement has already been linked to the build-up of protein aggregates based on impaired vesicular transport, in turn resulting in the activation of different cellular stress response mechanisms such as UPR and proteolysis (55) and, activation of UPR in mice was described to lead to premature neuron generation in the cerebral cortex and microcephaly (56). Moreover, several proteins involved in alternative splicing, mRNA stability and translational enhancers, including DDX3X, NCL, SRSF1, SSB, and FUS were found to be upregulated in a severity-dependent fashion, and an increased translation rate was also associated with ER stress. Notably, proteomic data unveiled significantly altered proteostasis in moderate and severe grade patient-derived organoids mirrored by a profound increase of different proteins involved in proteolysis and unfolded protein binding modulation, including BiP (the major chaperone resident in the ER) and its co-factor GRP170/ HYOU1 as well as HSP90-alpha, HSP90-beta and HSP90B1 (endoplasmin/ GRP94) along with the HSP90 co-chaperones CDC37 and DNAJC7. The two lectin chaperones calnexin and calreticulin, different protein disulfide-isomerases (PDIs), and DNAJC8, whose upregulation has already been associated with protective mechanisms in neurodegenerative diseases, including spinal degeneration, Parkinson and Machado-Joseph disease (57-60). Upregulation of these markers is consistent with increased folding activity in the ER. However, it cannot be excluded that it is also related to the activation of unfolded protein response. Activation of UPR is mediated by many posttranslational modifications, including phosphorylation of eIF2a and IRE1a and de-glycosylation of ATF6a (61), while our analysis could only detect changes in absolute protein levels. In summary, we observed severity-dependent changes in cytoarchitecture as well as RNA and protein expression levels, highlighting cytoskeletal destabilization and alterations in WNT-signalling and the spliceosome.

As proof of principle, we also showed that pharmacological treatment with the WNT agonist CHIR99021 partially rescues the severe grade phenotype, supporting the potentially critical role of this signaling pathway in the etiology of the severe form of the malformation. Similarly, the stabilization of microtubule arrays via EpothiloneD treatment ameliorated but did not fully recover the cellular structure of the VZ-like structures within organoids. This indicates that the severity-dependent phenotype is likely caused by a convergence of different

mechanisms, rather than by a single molecular pathway. To overcome this, and in an unbiased approach, we identified in an *in-silico* drug repurposing analysis, the FDA-approved drug everolimus that has been shown to reinstate TUBB2B and DCD2 levels, important interaction partners of LIS1 (62). As far as we know, this is the first time a connection has been made between LIS1 and mTOR signaling.

To our knowledge, this study is the first work using a combinatorial RNA-sequencing and proteomic approach that identifies altered gene expression and proteome in progenitor cells derived from patients affected by lissencephaly. Moreover, this study demonstrates the possibility of recapitulating different disease severity characteristics in cerebral organoids - a major challenge so far not addressed in the field - and shows that the organoid system is sensitive enough to decipher (molecular) pathologies with a wide spectrum of phenotypes affecting early human cortical development. In addition, our model not only provides an interesting proof of concept for *in silico* testing of potential drug candidates, but also a platform for future *in vitro* drug screening.

Acknowledgement

We thank Isabell Moskal, Helene Schamber and Elina Nürnberg for the pivotal technical support. We thank the DKFZ Single-Cell Open Lab (scOpenLab) for assistance with the scRNA sequencing experiment. We acknowledge the support of the NGS Core Facility Mannheim, Medical Faculty Mannheim of Heidelberg University.

Declarations

Funding

The work was supported by the Ministry of Innovation Science and Research of North Rhine-Westphalia (Junior Research Group, to J.L.), the ERA-NET NEURON, JTC 2015 Neurodevelopmental Disorders, STEM-MCD (to J.L., F.F. and N.B-B.) and the generous financial support by the Hector Stiftung II (to J.L.). A.He. gratefully acknowledges the financial support by the “Ministerium für Kultur und Wissenschaft des Landes Nordrhein-Westfalen,” the “Regierenden Bürgermeister von Berlin-Senatskanzlei Wissenschaft und Forschung,” and the “Bundesministerium für Bildung und Forschung.”

Competing Interests

The authors have no relevant financial or non-financial interests to disclose.

Author Contributions

Conceptualization, L.Z., A.C.R., O.F., S.G.M., P.K., F.F., and J.L.; Methodology, L.Z., A.C.R., O.F., M.G., C.M., A.Ho., E.Z., A.J., F.M., R.W., C.B.S., A.He., S.G.M., T.R., A.R., N.B-B. and J.L.; Validation, L.Z., A.C.R., O.F., M.G.; Formal Analysis, L.Z., O.F., M.G.; Investigation, L.Z., A.C.R., O.F.; ScRNA-Seq Data analysis, L.Z., E.Z. A.Ho., A.C.R., J.L.; mass spectrometry including data analyses C.B.S., A.He., T.R., A.R., M.G., L.Z., J.L., Whole-exome-sequencing, C.M. and N.B-B.; Writing – Original Draft, O.F., J.L.; Writing – Reviewing & Editing, L.Z., A.C.R., M.G., A.R., S.G.M., F.F. and J.L.; Visualization, L.Z., A.C.R., O.F. M.G, J.L.; Supervision, J.L.; Project Administration, J.L.; Funding Acquisition, N.B-B., F.F., J.L.

Data and code availability

Raw data will be made available through the European Genome-Phenome Archive. All original code has been deposited at GitHub repository and is publicly available as of the date of publication (https://github.com/lzillich/LIS1_code).

Inclusion and Ethics

For the human samples used in the study, all participants provided written informed consent prior to participation in the study. This study was ethically approved by the committees of the Imagine - Institut des maladies génétiques, Paris (approval number no. DC2014-2272) and by the Ethics Committee II of Medical Faculty Mannheim of Heidelberg University (approval no. 2014-626N-MA).

Materials and methods

Cell lines and patients

Control skin fibroblasts were obtained from Coriell Biorepository (control 1, 2-years old female, catalog ID GM00969, control 2, 5-month-old male, catalog ID GM08680). LIS1-patient fibroblasts and lymphocytes were collected from Nadia Bahi-Buisson from the Necker Enfants Malades University Hospital in France. We selected those LIS1 patients in this study for which blood and/or fibroblast samples were available, which were clinically and genetically well-characterized, for which high-quality MRI data were available, and for whom patient consent had been obtained. For more details see Philbert, Maillard (20) (LIS1-mild 1, 8-year-old male donor, c.569-10T>C LIS1 mutation; LIS1-mild 2, 5-year-old male donor, c.569-10T>C LIS1 mutation; LIS1-moderate 1, 6-year-old female donor, c.13delC LIS1 mutation; LIS1-moderate 2, 13-year-old female donor, delEx11 LIS1 mutation; LIS1-severe 1, 4-year-old female donor, c.1002+1G>T; LIS1-severe 2, 18-year-old female donor, c.531G>C LIS1-mutation; LIS1-severe 3, 3-yea-old female donor, c.445C>T LIS1 mutation). Each patient-specific LIS1 mutation was confirmed using Sanger sequencing after PCR amplification of the coding sequences. Induced PSC lines were generated with patient (caregiver) consent, and this study was ethically approved (Imagine – Institut des maladies génétiques, Paris; approval number no. DC2014-2272). In addition, 5 control iPS cell lines were received from Dr. Sandra Horschitz (Ethics Committee II of Medical Faculty Mannheim of Heidelberg University approval no. 2014-626N-MA, control 3, 21-year-old female donor; control 4, 44-year-old female donor; control 5, 25-year-old female donor; control 6, 26-year-old female donor, control 7, 23-year-old male donor). A complete overview of the cell lines used in this study is provided in Supplementary Text S1.

Reprogramming of fibroblasts and lymphocytes

Somatic cells were reprogrammed by non-integrative delivery of OCT4, SOX2, KLF4, and c-MYC using the CTS™ CytoTune™-iPS 2.1 Sendai Reprogramming Kit (Thermo Fisher). The manufacturer's instructions were strictly followed (CTS™ CytoTune™-iPS 2.1 Sendai Reprogramming Kit User Guide).

iPS cell validation and culture

Pluripotency of reprogrammed cells was quality-controlled by detection of the pluripotency-associated markers TRA-1-60, TRA-1-81, and SSEA-4 by immunocytochemistry and their capacity for spontaneous differentiation into cell types of all three germ layers. To induce 3-germ-layer differentiation iPSCs were dissociated into single cells using TrypLE Express and plated in an ultra-low-binding 96-well plate (9000 cells/well; Amsbio, lipidure-coat plate A-

U96) in Pluripro-medium (PP, Cell guidance systems) supplemented with 50 µM ROCK inhibitor to induce embryoid body (EB) formation. After 2 days, Ebs were plated onto extracellular matrix (GT)-coated dishes in DMEM containing 10% fetal calf serum (FCS), 1% pyruvate, and 1% non-essential amino acids (NEAA, Gibco). Cells were cultured for 4 weeks before being subjected to immunocytochemical analysis. Further whole-genome single nucleotide polymorphism (SNP) genotyping was performed for each iPS cell line for karyotyping. To that end, genomic DNA was prepared using the Dneasy Blood & Tissue Kit (Qiagen). SNP genotyping was performed at the Institute of Human Genetics at the University of Bonn. Genomic DNA at a concentration of 50 ng/µl was used for whole-genome amplification. Afterward, the amplified DNA was fragmented and hybridized to sequence-specific oligomers bound to beads on an Illumina OmniExpressExome v1.2 chip or Illumina Infinium PsychArray-24 v1.1 chip. Data were analyzed using Illumina GenomeStudio V2011.1 (Illumina). Patient-specific LIS1 mutations were validated in the iPS cells by Sanger sequencing for the LIS1-mutation c.13delC and c.569-10T>C, and in fibroblasts by Multiplex Ligation-dependent Probe Amplification (MLPA) for the LIS1-mutation: exon 11 del, c.1002+1G>T and c.445 C>T. Induced PS cells were maintained on Geltrex-coated cell culture plates (Thermo Fisher) in PP medium or Essential 8 (E8) medium at 37 °C, 5% CO2, and ambient oxygen level with daily medium change. For passaging cells were treated with TrypLE Express (Stem Cell Technologies) or EDTA (Thermo Fisher Scientific). After passaging, medium was supplemented with 5µM Y-27632 (CellGuidance Systems) to foster cell survival. All human iPS cell lines were regularly tested and confirmed negative for mycoplasma.

Generation of WNT-GFP reporter iPS cell lines

iPS cells were transduced with a Lentivirus expressing GFP under activation of WNT signaling (Lentiviral-Top-dGFP reporter, Addgene plasmid #14715). Puromycin (1µg/ml, Sigma-Aldrich) selection was initiated 48 h following transduction. iPS cell-WNT reporter lines were used for forebrain-type organoid generation.

Generation of 3D forebrain-type organoids and cortical progenitor cells.

Cerebral forebrain-type organoids were generated and quality controlled as previously described (13, 25). Briefly, iPS cell colonies were dissociated using TrypLE Express (Thermo Fisher Scientific) and cells were plated in u-bottom 96-well plates previously coated with 5% Pluronic F-127 (Sigma Aldrich) in phosphate-buffered saline (PBS). Cells were seeded in a volume of 150µl/well in PP or E8 medium supplemented with 50µM Y-27632. Following successful cell aggregation, medium was switched at day 5 to neural induction medium

(DMEM/F12, B27 supplement 1%, N2 supplement 0,5%v/v, cAMP 300ng/ml, GlutaMAX 1%, NEEA 1%, D-Glucose, Insulin, KOSR 2%, Penicillin/Streptomycin 1% v/v, heparin 1µg/ml, LDN-193189 0,2mM, A83-01 0,5mM and XAV 2µM) with a medium change every second day. Sufficient neural induction was monitored by the development of translucent and smooth edges using a bright field microscope. On days 9–11, when translucent neural ectoderm was visible, organoids were embedded in GT (Thermo Fisher), transferred to Pluronic F-127-coated dishes and maintained in neural differentiation medium (DMEM/F12, B27 supplement 1%, N2 supplement 0,5% v/v, cAMP 300ng/ml, GlutaMAX 1%, NEEA 1%, D-Glucose, Insulin, KOSR 2% and Penicillin Streptomycin 1% v/v). After this passage, organoids were kept in 10cm or 6cm dishes under agitation at 70rpm on an orbital shaker (Infors Celltron HD) at 37°C, 5% CO_2, and ambient oxygen level. Media was changed every 3 to 4 days. At day 15 or 20, organoids were harvested for phenotypical analysis, while for scRNA-seq they were collected at day 20+/-3. For immunostaining, 20µm sections were prepared using a cryotome. At least six organoids for each of three different batches were analyzed.

Induced PS cell-derived neural progenitors were generated along established protocols (25) with slide adaptations. Neural induction was initiated in 90-95% confluent iPS cell cultures by changing the culture medium to neural base medium containing advanced DMEM/F12 (Thermo Fisher Scientific, 12634010) supplemented with 1% Pen/Strep, Glutamax (1x; Thermo Fisher Scientific, 35050038) and 1% B-27 supplement (Thermo Fisher Scientific; 17504044). Cells were grown in neural base medium supplemented with SB-431542 (10 µM; Cell Guidance Systems, SM33), LDN-193189 (1 µM; StemCell Technologies, 72148) and XAV939 (2 µM; Cell Guidance Systems, SM38) for 8 days. On day 8 (in case of the LIS1 moderate line 1.2. on day 6 as this line tend to premature differentiate) neural progenitor base medium was supplemented with LDN-193189 (200 nM) and XAV939 (2 µM). Cells were harvested for mass spectrometry 2 days after passaging and replating in neural differentiation media containing DMEM/F12, 0.5% N2 supplement, 1% B27 supplement, and cAMP (300 ng/ml) on GT-coated cell culture plates. Cells cultured in parallel were used for quality control which include immunohistochemistry for neural progenitors and neurons. Only those batches where homogenous neural induction was confirmed were further processed for mass spectrometry. At least 4 samples derived from at least two different genetic backgrounds and generated from at least three different batches were processed for mass spectrometry.

CHIR and EpothiloneD Treatment

Organoids were treated after the induction phase, from culture day 10 to day 15. The drugs were resuspended in DMSO to reach the concentration of 1µM CHIR or 1nM EpothiloneD, respectively. After treatment, organoids were fixed and cryo-sectioned for immunocytochemical analysis.

Clearing of 3D forebrain-type organoids

For whole tissue mounting, organoids were fixed with 4% PFA for 2 h at RT and optically cleared according to Susaki et al. (63). Blocking was done with 10% horse serum, 0.2% gelatin from cold water fish skin, and 0.1% Triton X-100 diluted in PBS for 24 h at 37°C, followed by primary antibody incubation for 48 h at 37°C. Secondary antibody incubation was done for 48 h at 37°C. Refractive index matching was performed according to Nürnberg et al. (64) by immersion of samples in an aqueous solution of glycerol (RI=1.457) for 48 h at RT. Samples were mounted in U-shaped 2.5 mm glass capillaries by embedding in 0.1% low melting agarose in ddH_2O. For light sheet microscopy, glass capillaries were transferred into 35 mm glass bottom dishes, immobilized by agarose embedding, and immersed in RI-matched glycerol solution. For temperature adjustment, samples were kept in the microscopy room for at least 24 hours before image acquisition. Image acquisition was done using a Leica Microsystems TCS SP8 DLS, equipped with LAS X software, L 1.6x/0.05 DLS illumination objective, HC APO L 10x/0.30 W DLS detection objective and 7.8 mm Glycerol DLS TwinFlect mirrors. Image stacks were acquired with a step size of 3.7 µm and fused with LAS X.

Histology and Immunocytochemistry

Cells and organoids were fixed with 4% paraformaldehyde (PFA) for 10 min at room temperature (RT) and blocked in 10% Fetal Calf Serum in PBS with 0,1% Triton for 1 h at RT. Primary antibodies were diluted according to the manufacturer's instructions and incubated overnight at 4°C with the following dilutions: Ac-TUB (1:500, Cell signaling), AFP (1:200, Hölzel), TUBB3 (1:2000, Cell Signaling), NANOG (1:200, DSHB), N-CAD (1:500, BD), p-VIM (1:500, Novus biologicals), TPX2 (1:500, Novus Biologicals), OCT3/4 (1:500, R&D Systems), SMA (1:400, Abcam), SSEA3 (1:500, Abcam) and SOX2 (1:500, Santa Cruz), HSP90 (1:250, Genetex), BiP (1:250, provided by Professor Martin Jung, University of Saarland). The secondary antibodies were diluted according to the manufacturer's instructions and incubated for 1h at RT (488-ms/rb; 555-ms/rt; 647-ms,

1:1000, Invitrogen). Nuclei were visualized using 0,1µg/ml DAPI (Sigma Aldrich). Stained sections were stored at 4°C and imaged using the Inverted Leica DMIL LED Microscope with the Thunder imaging software (Leica).

Organoid quantifications

Organoid quantifications were performed as previously described (16) with slight adaptations. Images were acquired using the Inverted Leica DMIL LED Microscope with the Thunder imaging software (Leica) and analyzed using ImageJ software. All quantifications were done in at least three organoids with at least six VZ-like structures for each of at least three different organoid batches. The given n number is the total of VZ-like structures analyzed. For the quantification of the VZ dimension parameters, sections were stained with DAPI. Length and area measurements were performed with Image J software. For the VZ thickness, three measurements for each cortical VZ structure were performed: one straight measurement from the apical to the basal side of the VZ structure and two measurements both starting at the apical point of the first measurement while the basal point was located in a 45-degree angle on the right or left side. The mean of the three values was taken as VZ thickness. In the case of heterogenous VZ thickness, the thickest area was considered. The VZ tissue area was defined as the ratio of the total VZ area to the ventricle area. Ac-TUB strand density was measured by plot profile determination using ImageJ software and a self-designed Excel file containing formulae for background subtraction and automatic signal peak counting. The disruption diameter of N-CAD was measured at four apical membrane positions (90, 180, 270, and 360 degrees) using ImageJ software. The mean value was taken as disruption diameter. Mitotic spindles were analyzed by immunocytochemical staining using p-VIM for marking dividing RG cells at the apical membrane and TPX2 for the visualization of the mitotic spindle.

Cortical organoid dissociation for single-cell RNA-sequencing

20 +/- 3-day old organoids (two or three per condition: control C1, control C7, LIS1-mild P1, LIS1-mild P2, LIS1-moderate P3, LIS1-moderate P4 and LIS1 severe P5, LIS1-severe P6) were sliced with a scalpel and dissociated according to our already published protocol (25). Briefly, the tissue was incubated in papain (Sigma Aldrich) containing buffer (1mM L-cysteine and 0,5mM EDTA in Earle's balanced salt solution, 20 units of papain, and 10µg/ml of DNase (Sigma Aldrich) for 20 min at 37°C. After incubation, organoids were washed with

differentiation media and dissociated mechanically using a 1% bovine serum albumin (BSA)-coated 1000µl pipette. After centrifugation at 400g for 4 min at 4°C, the cell pellet was resuspended in 1ml ice-cold PBS supplemented with 0.04% BSA and filtered through a 30µm cell strainer. Single cell library preparation was performed using the 10x Genomics Chromium platform according to the 10x Genomics Chromium Single Cell 3' Library & Gel Bead Kit v3.1 chemistry user guide (10x Genomics). The prepared cDNA libraries were processed by the High Throughput Sequencing Unit of the Genomics & Proteomics Core Facility of the German Cancer Research Centre (DKFZ). The libraries were sequenced on two lanes of the Illumina NovaSeq 6k platform on a S1 flow cell (paired-end 28+94 bp).

ScRNA-seq data quality control and preprocessing

Count matrices for single-cell RNAseq data were generated from fastq files using cellranger (10x Genomics). Data analysis was performed using Seurat v.4.0.5 (65), if not stated otherwise. During quality control, features that were not expressed in any cell were removed from the count matrix. Next, cells were removed in each replicate individually based on the number of expressed features, total UMI counts, and mitochondrial gene fraction (>10%). For detailed QC parameters, see Sup. Table S17. For each sample, normalization was performed using *sctransform*. Cell cycle differences (S.Score-G2M.Score) were regressed out and cell multiplets were removed using the R package DoubletFinder v.2.0.3 (66). Integration of data was performed in two steps: first, for every condition, the two samples were integrated, followed by an integration of the four integrated objects resulting in the final Seurat object. UMAP dimensionality reduction and nearest-neighbor graph construction were performed based on dims 1:50. A resolution threshold of 0.15 was used for cluster generation. Cluster identity was determined based on the expression of known cell type markers. The intermediate progenitor (IP) cluster was manually split into two clusters according to normalized expression levels of the EOMES gene (>0.25) yielding a total of 10 clusters in the final object.

Sample preparation for mass spectrometry

Proteins from cortical progenitors were extracted from TriFast homogenized samples following manufacturer's protocol. Dried, snap-frozen protein pellets, underwent lysis through the addition of 200 µl of a 50 mM Tris-HCl buffer (pH 7.8) containing 5% SDS and cOmplete ULTRA protease inhibitor (Roche). The samples were then subjected to Bioruptor® treatment (Diagenode) for 10 minutes (30 sec on, 30 sec off, 10 cycles) at 4 °C, followed by centrifugation at 4 °C and 20,000 g for 15 minutes. Subsequently, the protein

concentration in the supernatant was determined using the BCA assay according to the manufacturer's guidelines. Disulfide bonds were reduced with the addition of 10 mM TCEP at 37 °C for 30 minutes, and free sulfhydryl bonds were alkylated with 15 mM IAA at room temperature in the dark for 30 minutes. For proteolysis, 100 µg of protein from each sample was utilized following the S-trap protocol (Protifi). The protein-to-trypsin ratio was maintained at 20:1, and digestion took place for 2 hours at 45 °C. The proteolysis process was terminated by acidifying the sample with formic acid (FA) to achieve a pH below 3.0. Verification of complete digestion of all proteolytic digests occurred post-desalting, utilizing monolithic column separation (PepSwift monolithic PS-DVB PL-CAP200-PM, Dionex) on an inert Ultimate 3000 HPLC (Dionex, Germering, Germany) through direct injection of 1 µg of the sample. A binary gradient (solvent A: 0.1% TFA, solvent B: 0.08% TFA, 84% ACN) ranging from 5-12% B in 5 minutes and then from 12-50% B in 15 minutes at a flow rate of 2.2 µL/min and at 60 °C was applied, with UV traces recorded at 214 nm (67).

Mass Spectrometry sample analysis

A total of 1 g of the respective peptide samples underwent separation using an Ultimate 3000 Rapid Separation Liquid Chromatography (RSLC) nano system equipped with a ProFlow flow control device, in conjunction with a Q Exactive HF Orbitrap mass spectrometer (Thermo Scientific, Schwerte, Germany). Peptide concentration employed a trapping column (Acclaim C18 PepMap100, 100 µm, 2 cm, Thermo Fisher Scientific, Schwerte, Germany) with 0.1% trifluoroacetic acid (TFA) from Sigma-Aldrich, Hamburg, Germany, at a flow rate of 10 L/min. Subsequent reversed-phase chromatography (Acclaim C18 PepMap100, 75 µm, 50 cm) utilized a binary gradient (solvent A: 0.1% formic acid (Sigma-Aldrich, Hamburg, Germany); solvent B: 84% acetonitrile (Sigma-Aldrich, Hamburg, Germany) with 0.1% formic acid; 5% B for 3 min, linear increase to 25% for 102 min, a further linear increase to 33% for 10 min, and a final linear increase to 95% for 2 min followed by a linear decrease to 5% for 5 min). For MS survey scans, the parameters included operating MS in data-dependent acquisition mode (DDA) with full MS scans from 300 to 1600 m/z (resolution 60,000) and the polysiloxane ion at 371.10124 m/z as a lock mass. The maximum injection time was set to 120 ms, and the automatic gain control (AGC) was set to 1E6. Fragmentation involved selecting the 15 most intense ions (above the threshold ion count of 5E3) at a normalized collision energy (nCE) of 27% in each cycle, following each survey scan. Fragment ions were acquired (resolution 15,000) with an AGC of 5E4 and a maximum injection time of 50 ms. Dynamic exclusion was set to 15 s.

Mass spectrometry data preprocessing

All MS raw data underwent processing using Proteome Discoverer software version 2.5.0.400 (Thermo Scientific, Bremen, Germany) and were subjected to a target/decoy mode search against a human Uniprot database (www.uniprot.org, downloaded on 21 November 2019) utilizing the MASCOT and Sequest algorithm. The search parameters included precursor and fragment ion tolerances of 10 ppm and 0.5 Da for MS and MS/MS, respectively. Trypsin was designated as the enzyme with a maximum of two allowed missed cleavages. Carbamidomethylation of cysteine was set as a fixed modification, and oxidation of methionine was set as a dynamic modification. Percolator false discovery rate (strict) was established at 0.01 for both peptide and protein identification. A Label-free Quantification (LFQ) analysis was conducted for proteins with a minimum of two unique peptides, encompassing replicates for each condition.

Statistical analysis

All statistical tests were performed two-sided with an alpha-error of 0.05 to indicate nominal statistical significance.

All quantitative data generated on organoids following immunocytochemistry was performed in batches of at least duplicates, at least two batches per cell line were analyzed. The number of included individual data points and batches can be found in the tables summarizing each statistical analysis. On average, we observed 6.26 individual data points per batch for VZ-like parameters, 4.07 for Ac-TUB, 3.67 for N-CAD disruption diameter, and 3 for cell division quantifications. During one routine karyotyping, we discovered abnormalities in cell line C2. Therefore, this cell line was excluded from all statistical analyses. Raw data was aggregated per batch, after which conditions were compared using Kruskal-Wallis- and *post-hoc*-pairwise Wilcoxon tests, as all observed parameters did not follow a gaussian distribution, which was tested using the Kolmogorov-Smirnov-Test. Differences in proportions were tested using Chi-Square tests. All results were corrected for multiple testing using the Bonferroni correction, if not stated otherwise.

For differential expression testing in the single cell sequencing data, an FDR-corrected p-value of 0.05 and an absolute log2FC larger than 0.5 was used to indicate statistical significance. Differential gene expression between the severities and the control condition in the progenitor cell populations (RG, NE, t-RG) was tested using the *FindMarkers()* function in Seurat, which encompasses a Wilcoxon Rank sum test. The minimum percentage of gene

expression was set to 0.25, meaning that a gene had to be expressed in at least 25% of cells in each population, therefore avoiding false positives by not testing genes with low expression.

Protein abundances were normalized, and log-transformed. To compare the severity grades with the control condition, Wilcoxon Rank sum tests were performed. Effect sizes were calculated by dividing the Z statistic through the square root of the sample size. FDR-correction was applied to correct for multiple testing and results were filtered for an absolute effect size larger than 0.75. In addition to testing differential protein regulation, we performed a weighted correlation network analysis using WGCNA (version 1.72-1) (68). Here, networks of co-regulated proteins are constructed based on the covariance of the normalized protein abundances. We used a soft threshold of 8, a signed TOM matrix, a minimum module size of 30 and a maximum block size of 20,000 to construct the modules. In WGCNA, modules are assigned random colors. Module eigengenes were correlated with the disease severities compared to the control condition. For significantly associated modules, in at least one of the conditions, a GO enrichment analysis was performed using the approach described below. For module hubgenes of the LIS1-associated modules, we constructed protein-protein interaction networks using the STRING database (v.11.5) (69).

Integrative Gene Ontology enrichment analysis of cellular pathways (GO) Biological Processes and Molecular Functions) of differentially regulated genes ($p_{adj}<0.05$) and proteins ($p<0.05$) was determined using the enrichGO() and compareCluster() functions of the R package clusterProfiler (v. 4.6.2). For this purpose, genes contributing to a GO term were retrieved using the org.Hs.eg.db package (v.3.14.0). We determined semantic overlap of enriched GO-terms using the pairwise_termsim() function of enrichplot (v.1.18.3) and visualized the results using the emapplot() function of the same package.

Drug repositioning analysis

The NIH LINCS L1000 database (70) was used as a reference dataset for drug repositioning analysis in connectivity map analysis (CMap, https://clue.io, software version 1.1.1.43). The top 150 upregulated and downregulated DE genes from the RG cluster were used to generate the maximum input size for the CMap query tool. CMap allows an *in-silico* drug repositioning analysis by comparing expression changes of n=978 landmark transcripts in response to standardized drug treatment protocols against the query differential expression signature. Resulting connectivity scores indicate rescue (negative score) or aggravation (positive score) of queried transcriptional changes by drug treatment. Next to the generation of connectivity scores for individual drugs or more general *"perturbagens"*, CMAP also

provides connectivity information at the perturbagen class, mechanism of action, and pathway level thus enabling a more general understanding of potential therapeutic targets in a phenotype. For visualization of CMap results, waterfall plots were generated using ggplot2 (v.3.4.2). Results for individual perturbagens such as pharmaceutical drugs or gene products were filtered based on negative normalized connectivity scores (NCS<0) in all three conditions (mild, moderate, severe). Mechanism of action (MOA) results were filtered based on negative normalized connectivity scores in at least two conditions (moderate and severe).

References

1. Florio M, Huttner WB. Neural progenitors, neurogenesis and the evolution of the neocortex. Development. 2014;141(11):2182-94.

2. Severino M, Geraldo AF, Utz N, Tortora D, Pogledic I, Klonowski W, et al. Definitions and classification of malformations of cortical development: practical guidelines. Brain. 2020;143(10):2874-94.

3. Francis F, Meyer G, Fallet-Bianco C, Moreno S, Kappeler C, Socorro AC, et al. Human disorders of cortical development: from past to present. Eur J Neurosci. 2006;23(4):877-93.

4. Koenig M, Dobyns WB, Di Donato N. Lissencephaly: Update on diagnostics and clinical management. Eur J Paediatr Neurol. 2021;35:147-52.

5. de Wit MC, de Rijk-van Andel J, Halley DJ, Poddighe PJ, Arts WF, de Coo IF, et al. Long-term follow-up of type 1 lissencephaly: survival is related to neuroimaging abnormalities. Dev Med Child Neurol. 2011;53(5):417-21.

6. Saillour Y, Carion N, Quelin C, Leger PL, Boddaert N, Elie C, et al. LIS1-related isolated lissencephaly: spectrum of mutations and relationships with malformation severity. Arch Neurol. 2009;66(8):1007-15.

7. Faulkner NE, Dujardin DL, Tai CY, Vaughan KT, O'Connell CB, Wang Y, et al. A role for the lissencephaly gene LIS1 in mitosis and cytoplasmic dynein function. Nat Cell Biol. 2000;2(11):784-91.

8. Smith DS, Niethammer M, Ayala R, Zhou Y, Gambello MJ, Wynshaw-Boris A, et al. Regulation of cytoplasmic dynein behaviour and microtubule organization by mammalian Lis1. Nat Cell Biol. 2000;2(11):767-75.

9. Yingling J, Youn YH, Darling D, Toyo-Oka K, Pramparo T, Hirotsune S, et al. Neuroepithelial stem cell proliferation requires LIS1 for precise spindle orientation and symmetric division. Cell. 2008;132(3):474-86.

10. Moon HM, Youn YH, Pemble H, Yingling J, Wittmann T, Wynshaw-Boris A. LIS1 controls mitosis and mitotic spindle organization via the LIS1-NDEL1-dynein complex. Hum Mol Genet. 2014;23(2):449-66.

11. Youn YH, Pramparo T, Hirotsune S, Wynshaw-Boris A. Distinct dose-dependent cortical neuronal migration and neurite extension defects in Lis1 and Ndel1 mutant mice. J Neurosci. 2009;29(49):15520-30.

12. Gambello MJ, Darling DL, Yingling J, Tanaka T, Gleeson JG, Wynshaw-Boris A. Multiple dose-dependent effects of Lis1 on cerebral cortical development. J Neurosci. 2003;23(5):1719-29.

13. Krefft O, Jabali A, Iefremova V, Koch P, Ladewig J. Generation of Standardized and Reproducible Forebrain-type Cerebral Organoids from Human Induced Pluripotent Stem Cells. J Vis Exp. 2018(131).

14. Quadrato G, Nguyen T, Macosko EZ, Sherwood JL, Min Yang S, Berger DR, et al. Cell diversity and network dynamics in photosensitive human brain organoids. Nature. 2017;545(7652):48-53.

15. Camp JG, Badsha F, Florio M, Kanton S, Gerber T, Wilsch-Bräuninger M, et al. Human cerebral organoids recapitulate gene expression programs of fetal neocortex development. Proc Natl Acad Sci U S A. 2015;112(51):15672-7.

16. Iefremova V, Manikakis G, Krefft O, Jabali A, Weynans K, Wilkens R, et al. An Organoid-Based Model of Cortical Development Identifies Non-Cell-Autonomous Defects in Wnt Signaling Contributing to Miller-Dieker Syndrome. Cell Rep. 2017;19(1):50-9.

17. Bershteyn M, Nowakowski TJ, Pollen AA, Di Lullo E, Nene A, Wynshaw-Boris A, et al. Human iPSC-Derived Cerebral Organoids Model Cellular Features of Lissencephaly and Reveal Prolonged Mitosis of Outer Radial Glia. Cell Stem Cell. 2017;20(4):435-49.e4.

18. Sapir T, Eisenstein M, Burgess HA, Horesh D, Cahana A, Aoki J, et al. Analysis of lissencephaly-causing LIS1 mutations. Eur J Biochem. 1999;266(3):1011-20.

19. Barkovich AJ, Guerrini R, Kuzniecky RI, Jackson GD, Dobyns WB. A developmental and genetic classification for malformations of cortical development: update 2012. Brain. 2012;135(Pt 5):1348-69.

20. Philbert M, Maillard C, Cavallin M, Goldenberg A, Masson C, Boddaert N, et al. A novel recurrent LIS1 splice site mutation in classic lissencephaly. Am J Med Genet A. 2017;173(2):561-4.

21. Pollen AA, Nowakowski TJ, Chen J, Retallack H, Sandoval-Espinosa C, Nicholas CR, et al. Molecular identity of human outer radial glia during cortical development. Cell. 2015;163(1):55-67.

22. Nowakowski TJ, Bhaduri A, Pollen AA, Alvarado B, Mostajo-Radji MA, Di Lullo E, et al. Spatiotemporal gene expression trajectories reveal developmental hierarchies of the human cortex. Science. 2017;358(6368):1318-23.

23. Liu J, Liu W, Yang L, Wu Q, Zhang H, Fang A, et al. The Primate-Specific Gene TMEM14B Marks Outer Radial Glia Cells and Promotes Cortical Expansion and Folding. Cell Stem Cell. 2017;21(5):635-49.e8.

24. Velasco S, Kedaigle AJ, Simmons SK, Nash A, Rocha M, Quadrato G, et al. Individual brain organoids reproducibly form cell diversity of the human cerebral cortex. Nature. 2019;570(7762):523-7.

25. Jabali A, Hoffrichter A, Uzquiano A, Marsoner F, Wilkens R, Siekmann M, et al. Human cerebral organoids reveal progenitor pathology in EML1-linked cortical malformation. EMBO Rep. 2022;23(5):e54027.

26. Harrison-Uy SJ, Pleasure SJ. Wnt signaling and forebrain development. Cold Spring Harb Perspect Biol. 2012;4(7):a008094.

27. Liu SJ, Nowakowski TJ, Pollen AA, Lui JH, Horlbeck MA, Attenello FJ, et al. Single-cell analysis of long non-coding RNAs in the developing human neocortex. Genome Biol. 2016;17:67.

28. Assis-Mendonça GR, Athié MCP, Tamanini JVG, de Souza A, Zanetti GG, Araújo P, et al. Transcriptome analyses of the cortex and white matter of focal cortical dysplasia type II: Insights into pathophysiology and tissue characterization. Front Neurol. 2023;14:1023950.

29. Zárate SC, Traetta ME, Codagnone MG, Seilicovich A, Reinés AG. Humanin, a Mitochondrial-Derived Peptide Released by Astrocytes, Prevents Synapse Loss in Hippocampal Neurons. Front Aging Neurosci. 2019;11:123.

30. Pitale PM, Howse W, Gorbatyuk M. Neuronatin Protein in Health and Disease. J Cell Physiol. 2017;232(3):477-81.

31. Montalbán-Loro R, Lassi G, Lozano-Ureña A, Perez-Villalba A, Jiménez-Villalba E, Charalambous M, et al. Dlk1 dosage regulates hippocampal neurogenesis and cognition. Proc Natl Acad Sci U S A. 2021;118(11).

32. Uren A, Reichsman F, Anest V, Taylor WG, Muraiso K, Bottaro DP, et al. Secreted frizzled-related protein-1 binds directly to Wingless and is a biphasic modulator of Wnt signaling. J Biol Chem. 2000;275(6):4374-82.

33. Muralidharan B, Khatri Z, Maheshwari U, Gupta R, Roy B, Pradhan SJ, et al. LHX2 Interacts with the NuRD Complex and Regulates Cortical Neuron Subtype Determinants Fezf2 and Sox11. J Neurosci. 2017;37(1):194-203.

34. Hou PS, hAilín D, Vogel T, Hanashima C. Transcription and Beyond: Delineating FOXG1 Function in Cortical Development and Disorders. Front Cell Neurosci. 2020;14:35.

35. Ladewig J, Koch P, Brüstle O. Auto-attraction of neural precursors and their neuronal progeny impairs neuronal migration. Nat Neurosci. 2014;17(1):24-6.

36. Kshirsagar A, Doroshev SM, Gorelik A, Olender T, Sapir T, Tsuboi D, et al. LIS1 RNA-binding orchestrates the mechanosensitive properties of embryonic stem cells in AGO2-dependent and independent ways. Nat Commun. 2023;14(1):3293.

37. Parada CA, Roeder RG. A novel RNA polymerase II-containing complex potentiates Tat-enhanced HIV-1 transcription. Embo j. 1999;18(13):3688-701.

38. Gong C, Krupka JA, Gao J, Grigoropoulos NF, Giotopoulos G, Asby R, et al. Sequential inverse dysregulation of the RNA helicases DDX3X and DDX3Y facilitates MYC-driven lymphomagenesis. Mol Cell. 2021;81(19):4059-75.e11.

39. Maayan Karlinski Z, Bidisha B, Sivan Ben D, Inna S, Alon S, Tamar S, et al. Altered Extracellular Matrix Structure and Elevated Stiffness in a Brain Organoid Model for Disease. bioRxiv. 2024:2024.01.09.574777.

40. Giannakakou P, Gussio R, Nogales E, Downing KH, Zaharevitz D, Bollbuck B, et al. A common pharmacophore for epothilone and taxanes: molecular basis for drug resistance conferred by tubulin mutations in human cancer cells. Proc Natl Acad Sci U S A. 2000;97(6):2904-9.

41. Fumoleau P, Coudert B, Isambert N, Ferrant E. Novel tubulin-targeting agents: anticancer activity and pharmacologic profile of epothilones and related analogues. Ann Oncol. 2007;18 Suppl 5:v9-15.

42. Bollag DM, McQueney PA, Zhu J, Hensens O, Koupal L, Liesch J, et al. Epothilones, a new class of microtubule-stabilizing agents with a taxol-like mechanism of action. Cancer Res. 1995;55(11):2325-33.

43. Pachenari N, Kiani S, Javan M. Inhibition of glycogen synthase kinase 3 increased subventricular zone stem cells proliferation. Biomed Pharmacother. 2017;93:1074-82.

44. de Jonge M, Verweij J. The epothilone dilemma. J Clin Oncol. 2005;23(36):9048-50.

45. Guarnieri FC, de Chevigny A, Falace A, Cardoso C. Disorders of neurogenesis and cortical development. Dialogues Clin Neurosci. 2018;20(4):255-66.

46. D'Gama AM, Walsh CA. Somatic mosaicism and neurodevelopmental disease. Nat Neurosci. 2018;21(11):1504-14.

47. Mary S, Charrasse S, Meriane M, Comunale F, Travo P, Blangy A, et al. Biogenesis of N-cadherin-dependent cell-cell contacts in living fibroblasts is a microtubule-dependent kinesin-driven mechanism. Mol Biol Cell. 2002;13(1):285-301.

48. Hatakeyama J, Wakamatsu Y, Nagafuchi A, Kageyama R, Shigemoto R, Shimamura K. Cadherin-based adhesions in the apical endfoot are required for active Notch signaling to control neurogenesis in vertebrates. Development. 2014;141(8):1671-82.

49. Kadowaki M, Nakamura S, Machon O, Krauss S, Radice GL, Takeichi M. N-cadherin mediates cortical organization in the mouse brain. Dev Biol. 2007;304(1):22-33.

50. Zhang J, Woodhead GJ, Swaminathan SK, Noles SR, McQuinn ER, Pisarek AJ, et al. Cortical neural precursors inhibit their own differentiation via N-cadherin maintenance of beta-catenin signaling. Dev Cell. 2010;18(3):472-9.

51. Da Silva F, Zhang K, Pinson A, Fatti E, Wilsch-Bräuninger M, Herbst J, et al. Mitotic WNT signalling orchestrates neurogenesis in the developing neocortex. EMBO J. 2021;40(19):e108041.

52. Moon HM, Hippenmeyer S, Luo L, Wynshaw-Boris A. LIS1 determines cleavage plane positioning by regulating actomyosin-mediated cell membrane contractility. Elife. 2020;9.

53. Uzquiano A, Gladwyn-Ng I, Nguyen L, Reiner O, Götz M, Matsuzaki F, et al. Cortical progenitor biology: key features mediating proliferation versus differentiation. J Neurochem. 2018;146(5):500-25.

54. Kalebic N, Huttner WB. Basal Progenitor Morphology and Neocortex Evolution. Trends Neurosci. 2020;43(11):843-53.

55. Hentschel A, Meyer N, Kohlschmidt N, Groß C, Sickmann A, Schara-Schmidt U, et al. A Homozygous PPP1R21 Splice Variant Associated with Severe Developmental Delay, Absence of Speech, and Muscle Weakness Leads to Activated Proteasome Function. Mol Neurobiol. 2023;60(5):2602-18.

56. Laguesse S, Creppe C, Nedialkova DD, Prévot PP, Borgs L, Huysseune S, et al. A Dynamic Unfolded Protein Response Contributes to the Control of Cortical Neurogenesis. Dev Cell. 2015;35(5):553-67.

57. Rao RV, Bredesen DE. Misfolded proteins, endoplasmic reticulum stress and neurodegeneration. Curr Opin Cell Biol. 2004;16(6):653-62.

58. Jin H, Mimura N, Kashio M, Koseki H, Aoe T. Late-onset of spinal neurodegeneration in knock-in mice expressing a mutant BiP. PLoS One. 2014;9(11):e112837.

59. Melo EP, Konno T, Farace I, Awadelkareem MA, Skov LR, Teodoro F, et al. Stress-induced protein disaggregation in the endoplasmic reticulum catalysed by BiP. Nat Commun. 2022;13(1):2501.

60. Ito N, Kamiguchi K, Nakanishi K, Sokolovskya A, Hirohashi Y, Tamura Y, et al. A novel nuclear DnaJ protein, DNAJC8, can suppress the formation of spinocerebellar ataxia 3 polyglutamine aggregation in a J-domain independent manner. Biochem Biophys Res Commun. 2016;474(4):626-33.

61. Hetz C, Zhang K, Kaufman RJ. Mechanisms, regulation and functions of the unfolded protein response. Nat Rev Mol Cell Biol. 2020;21(8):421-38.

62. Jeruschke S, Jeruschke K, DiStasio A, Karaterzi S, Büscher AK, Nalbant P, et al. Everolimus Stabilizes Podocyte Microtubules via Enhancing TUBB2B and DCDC2 Expression. PLoS One. 2015;10(9):e0137043.

63. Susaki EA, Tainaka K, Perrin D, Kishino F, Tawara T, Watanabe TM, et al. Whole-brain imaging with single-cell resolution using chemical cocktails and computational analysis. Cell. 2014;157(3):726-39.

64. Nürnberg E, Vitacolonna M, Klicks J, von Molitor E, Cesetti T, Keller F, et al. Routine Optical Clearing of 3D-Cell Cultures: Simplicity Forward. Front Mol Biosci. 2020;7:20.

65. Hao Y, Hao S, Andersen-Nissen E, Mauck WM, Zheng S, Butler A, et al. Integrated analysis of multimodal single-cell data. Cell. 2021;184(13):3573-87.e29.

66. McGinnis CS, Murrow LM, Gartner ZJ. DoubletFinder: Doublet Detection in Single-Cell RNA Sequencing Data Using Artificial Nearest Neighbors. Cell Syst. 2019;8(4):329-37.e4.

67. Burkhart JM, Schumbrutzki C, Wortelkamp S, Sickmann A, Zahedi RP. Systematic and quantitative comparison of digest efficiency and specificity reveals the impact of trypsin quality on MS-based proteomics. J Proteomics. 2012;75(4):1454-62.

68. Langfelder P, Horvath S. WGCNA: an R package for weighted correlation network analysis. BMC Bioinformatics. 2008;9:559.

69. Szklarczyk D, Gable AL, Nastou KC, Lyon D, Kirsch R, Pyysalo S, et al. The STRING database in 2021: customizable protein-protein networks, and functional

characterization of user-uploaded gene/measurement sets. Nucleic Acids Res. 2021;49(D1):D605-d12.

70. Subramanian A, Narayan R, Corsello SM, Peck DD, Natoli TE, Lu X, et al. A Next Generation Connectivity Map: L1000 Platform and the First 1,000,000 Profiles. Cell. 2017;171(6):1437-52.e17.

Figure Captions

Fig. 1 Organoid morphology can be correlated with LIS1 patient severity grades. **A**) Representative brightfield images of control C1.2, mild P1.1, moderate P3.1 and severe P5.1 LIS1 patient-derived organoids at day 20. The black box indicates the area enlarged on the right. **B**) Representative light sheet microscopy (LSM) pictures of whole-tissue cleared control C2.1, mild P1.1, moderate P3.2 and severe P5.1 patient-derived organoids at day 20, stained for ß-III Tubulin (TUBB3). **C**) Representative Hoechst staining of ventricular zone structures (VZ) of control C1.2, mild P1.1, moderate P3.1 and severe P5.1 patient-derived organoids at day 20. Yellow dotted lines define the VZ areas. **D**) Quantification of VZ thickness (top) and length of apical membrane (bottom) in control and LIS1 patient-derived organoids at day 20. Central line in boxplot represents median, lower the 25th and upper lines the 75th percentile, Whiskers are 1.5 interquartile ranges. Individual dots represent the mean of one batch. (**E-G**) Representative staining of later stage control, mild, moderate and severe grade patient-derived organoids at day 58+/-2 for the bRG marker PTPRZ1 (**E**) and FAM107A (**F)**; E-F: co-stained with phosphorylated VIMENTIN (p-VIM) and counterstained with Hoechst) and the cortical neuronal layer specific markers TBR1, CTIP2 and SATB2 (**G,** counterstained with Hoechst). Scale bars, (A, B) 200 µm (C, E, F, G) 50 µm. Error bars, ±SD. *P< 0.05, **P< 0.01, ***P< 0.001.

Fig. 2 Multi-omics analyses suggest shared and severity-specific molecular alterations underlying the phenotypic changes across the different LIS1-severity grades. **(A)** Schematic representation of the scRNAseq and mass spectrometry experiments. **(B)** UMAP dimensional reduction and unbiased clustering reveals 10 distinct color-coded cell populations within control, mild-, moderate- and severe LIS1 patient-derived organoids: neuroepithelial cells (NE), cycling progenitors (CyP), radial glia cells (RG), intermediate progenitors (IP), transitory RG (t-RG), dorsal forebrain (dFB-N), ventral forebrain (vFB-N), midbrain (MB-N), interneurons (IN) and glial cells (G). **(C)** Cell type distribution in each severity grade. **(D)** Violin plots depicting scores of GO terms differentiating t-RG from RG cells, ***P< 0.001. **(E)** Heatmap depicting differentially expressed genes between the control and the mild, moderate, and severe severity-grades (adjusted p value < .05 and absolute log2FC > .50). Annotated are the 10 unique genes with the smallest p value per condition. Color intensity refers to the strength of association (log2FC). **(F)** Heatmap depicting log2FC (RNA) and Wilcoxon's r (protein) between the severity grades and the control condition, for LIS1 interaction partners. **(G)** Heatmap depicting the correlations of module eigengenes from WGCNA modules and severity grades. **(H)** String network of proteins included in the blue module. Proteins have been clustered by MCL clustering with the inflation parameter set to 3. Edges represent the degree of confidence for the interaction and only proteins forming proteins with a high degree of confidence (interaction score ≥ 0.700) have been plotted. Red cluster: associated with mRNA splicing. Yellow cluster: involvement in cytoplasmic translation and rRNA processing. Sage green: involved in protein folding in the endoplasmic reticulum. Mint and dark green clusters: associated with

the regulation of cell shape and chromatin assembly. **(J)** Emap plot of GO biological processes overrepresented in differentially regulated genes and proteins, showing five categories, size of circles representing the number of differentially regulated features in GO term.

Fig. 3 Probing selective molecular pathways identified in the OMICS analyses in LIS1-pateint-derived organoids. (A) Bar graphs depicting the -log10-transformed p values of the GO molecular function enrichment analysis, for the GO terms acting binding, actin filament binding, tubulin binding, and structural constituent of cytoskeleton, for differentially regulated genes (reds) and proteins (blues), solid line represents p values threshold .05 and dotted line the Bonferroni-adjusted p value threshold. (**B**) Representative images of whole-tissue cleared (first column, scale bar 200 µm) or cryo-sectioned (second and third column, scale bar 50 µm) organoids stained for acetylated α-tubulin (Ac-TUB). Control (C4.1), mild (P1.1), moderate (P3.2) and severe (P5.2) LIS1-patient derived organoids at day 20. (**C**) Quantification of apical and basal Ac-TUB strand density in control, mild, moderate and severe LIS1 patient-derived organoids at day 20, statistical analyses in Sup. Table S11. (**D**) Representative images of control (C3.1), mild (P2.1), moderate (P3.2) and severe (P5.1) patient-derived organoids stained for N-cadherin (N-CAD) at day 20. **(E**) Quantification of apical N-CAD signal in control, mild, moderate, and severe LIS1 patient-derived organoids at day 20, statistical analyses in Sup. Table S12, scale bar 20 µm. **(F)** Bar graph depicting the -log10-transformed p values of the GO enrichment analysis of the term cadherin binding, for differentially regulated genes (reds) and proteins (blues), solid line represents p values threshold .05 and dotted line the Bonferroni-adjusted p value threshold. (**G**) Representative images of WNT-GFP reporter control (C3.1), mild (P1.1), moderate (P3.1) and severe (P5.1) patient-derived organoids at day 20. **H**) Quantification of mean value of WNT-GFP signal in VZ structures, control N=20, mild N=20, moderate N=10, severe N=10.; scale bar 50 µm. Error bars, ±SD. **(J)** Relative quantification of cell division plane orientation at day 20, control N=14, mild N=56, moderate N=43, severe N=57 and **(K)** Representative magnifications of vertical, horizontal and oblique division planes in control (C4.1) and severe LIS1 (P5.1) patient-derived organoids. (**L**) Heatmap showing the log2FC of differentially expressed genes belonging to WNT signaling pathway in the CyP population of each severity-grade group compared to control. *P< 0.05, **P< 0.01, ***P< 0.001.

Fig. 4 Probing therapeutic targets in LIS1 patient-derived organoids. (A) Quantification of basal Ac-TUB strand density in DMSO and Epothilone D (EpoD, 1nM) treated control and LIS1-patient derived organoids at day 15, statistical analyses in Sup. Table S13. (**B**) VZ thickness quantification of DMSO and EpoD treated control- and LIS1 patient-derived organoids at day 15, statistical analyses in Sup. Table S14. Central line in boxplot represents median, lower the 25th and upper lines the 75th percentile, Whiskers are 1.5 interquartile ranges. Individual dots represent the mean of one batch (≥ 2 replicates). (**C**) Representative Hoechst staining of control (C3.1), mild (P1.1), moderate (P3.2) and severe (P5.1)

LIS1-patient derived organoids treated with DMSO or EpoD. The yellow dotted lines indicate the edges of the VZ areas, the green dotted lines those of the cortical plate regions, and the green arrows illustrates the cortical plate thickness. Scale bars 200 µm. (**D**) Quantification of N-CAD diameter expansion in DMSO and EpoD treated control and LIS1-patient derived organoids at day 15, statistical analyses in Sup. Table S15. Central line in boxplot represents median, lower the 25th and upper lines the 75th percentile, Whiskers are 1.5 interquartile ranges. Individual dots represent each loops measurement. (**E**) Representative N-cadherin (N-CAD) staining of mild, moderate and severe LIS1 patient-derived organoids treated with DMSO or EpoD. Yellow dotted lines define the VZ areas. Scale bars 20µm. (**F**) Representative DAPI images of control (C3.1), mild (P1.1), moderate (P4.2) and severe (P6.1) LIS1 patient-derived organoids treated with DMSO or CHIR99021 (CHIR, 1µM). The yellow dotted lines indicate the edges of the VZ areas, the blue dotted lines those of the cortical plate regions, and the blue arrows illustrates the cortical plate thickness. Scale bars 200 µm. **(G**) VZ thickness quantification of DMSO and CHIR treated organoids. Central line in boxplot represents median, lower the 25th and upper lines the 75th percentile, Whiskers are 1.5 interquartile ranges. Individual dots represent the mean of one batch (≥ 2 replicates). (**H**) Quantification of cell division plane orientation in control and LIS1-patient derived organoids treated with DMSO or CHIR, statistical analyses in Sup. Table Error bars, ±SD. *P< 0.05, **P< 0.01, ***P< 0.001.

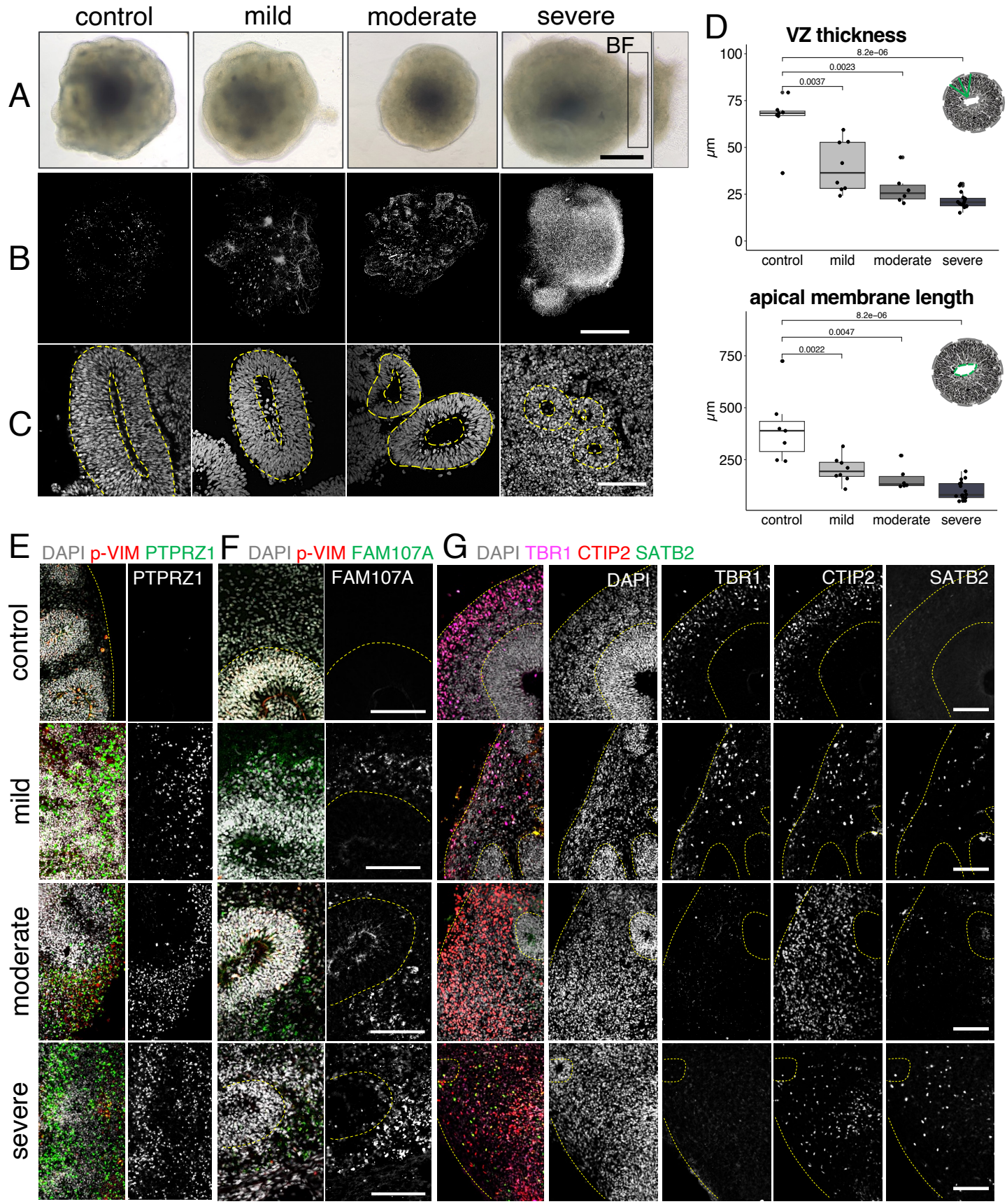
control
mild
moderate
severe
A
BF
B
C
D
VZ thickness
8.2e−06
0.0023
0.0037
100
75
50
25
0
μm
control
mild
moderate
severe
apical membrane length
8.2e−06
0.0047
0.0022
750
500
250
μm
control
mild
moderate
severe
E
DAPI p-VIM PTPRZ1
PTPRZ1
F
DAPI p-VIM FAM107A
FAM107A
G
DAPI TBR1 CTIP2 SATB2
DAPI
TBR1
CTIP2
SATB2
control
mild
moderate
severe

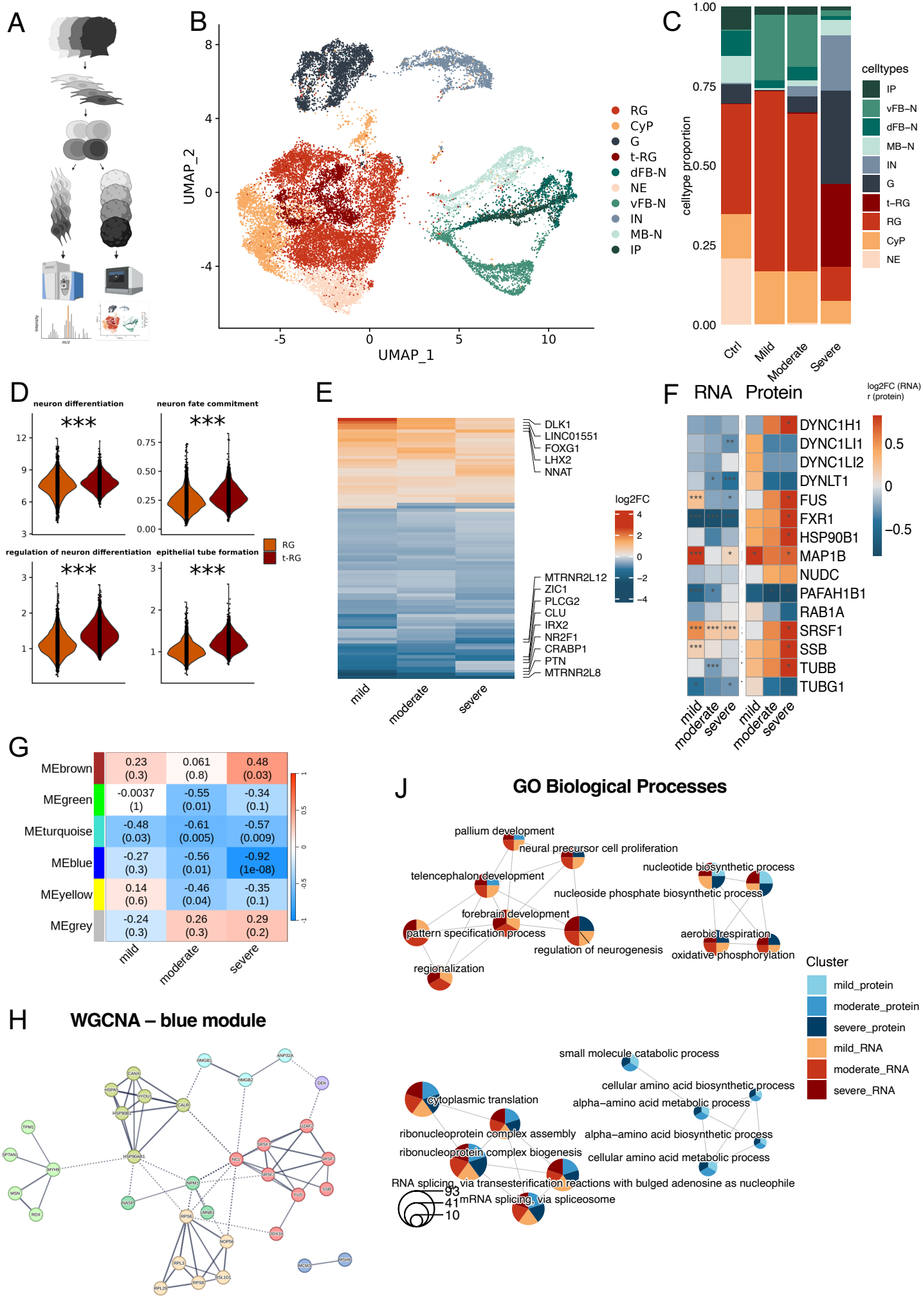
A
B
UMAP_2
UMAP_1
RG
CyP
G
t-RG
dFB-N
NE
vFB-N
IN
MB-N
IP
C
celltype proportion
celltypes
Ctrl
Mild
Moderate
Severe
D
neuron differentiation
neuron fate commitment
regulation of neuron differentiation
epithelial tube formation
RG
t-RG
E
log2FC
DLK1
LINC01551
FOXG1
LHX2
NNAT
MTRNR2L12
ZIC1
PLCG2
CLU
IRX2
NR2F1
CRABP1
PTN
MTRNR2L8
mild
moderate
severe
F
RNA
Protein
log2FC (RNA)
r (protein)
DYNC1H1
DYNC1LI1
DYNC1LI2
DYNLT1
FUS
FXR1
HSP90B1
MAP1B
NUDC
PAFAH1B1
RAB1A
SRSF1
SSB
TUBB
TUBG1
G
MEbrown
MEgreen
MEturquoise
MEblue
MEyellow
MEgrey
0.23 (0.3)
0.061 (0.8)
0.48 (0.03)
-0.0037 (1)
-0.55 (0.01)
-0.34 (0.1)
-0.48 (0.03)
-0.61 (0.005)
-0.57 (0.009)
-0.27 (0.3)
-0.56 (0.01)
-0.92 (1e-08)
0.14 (0.6)
-0.46 (0.04)
-0.35 (0.1)
-0.24 (0.3)
0.26 (0.3)
0.29 (0.2)
mild
moderate
severe
J
GO Biological Processes
pallium development
neural precursor cell proliferation
telencephalon development
forebrain development
pattern specification process
regionalization
regulation of neurogenesis
nucleotide biosynthetic process
nucleoside phosphate biosynthetic process
aerobic respiration
oxidative phosphorylation
Cluster
mild_protein
moderate_protein
severe_protein
mild_RNA
moderate_RNA
severe_RNA
H
WGCNA – blue module
small molecule catabolic process
cellular amino acid biosynthetic process
alpha−amino acid metabolic process
alpha−amino acid biosynthetic process
cellular amino acid metabolic process
cytoplasmic translation
ribonucleoprotein complex assembly
ribonucleoprotein complex biogenesis
RNA splicing, via transesterification reactions with bulged adenosine as nucleophile
mRNA splicing, via spliceosome
93
41
10

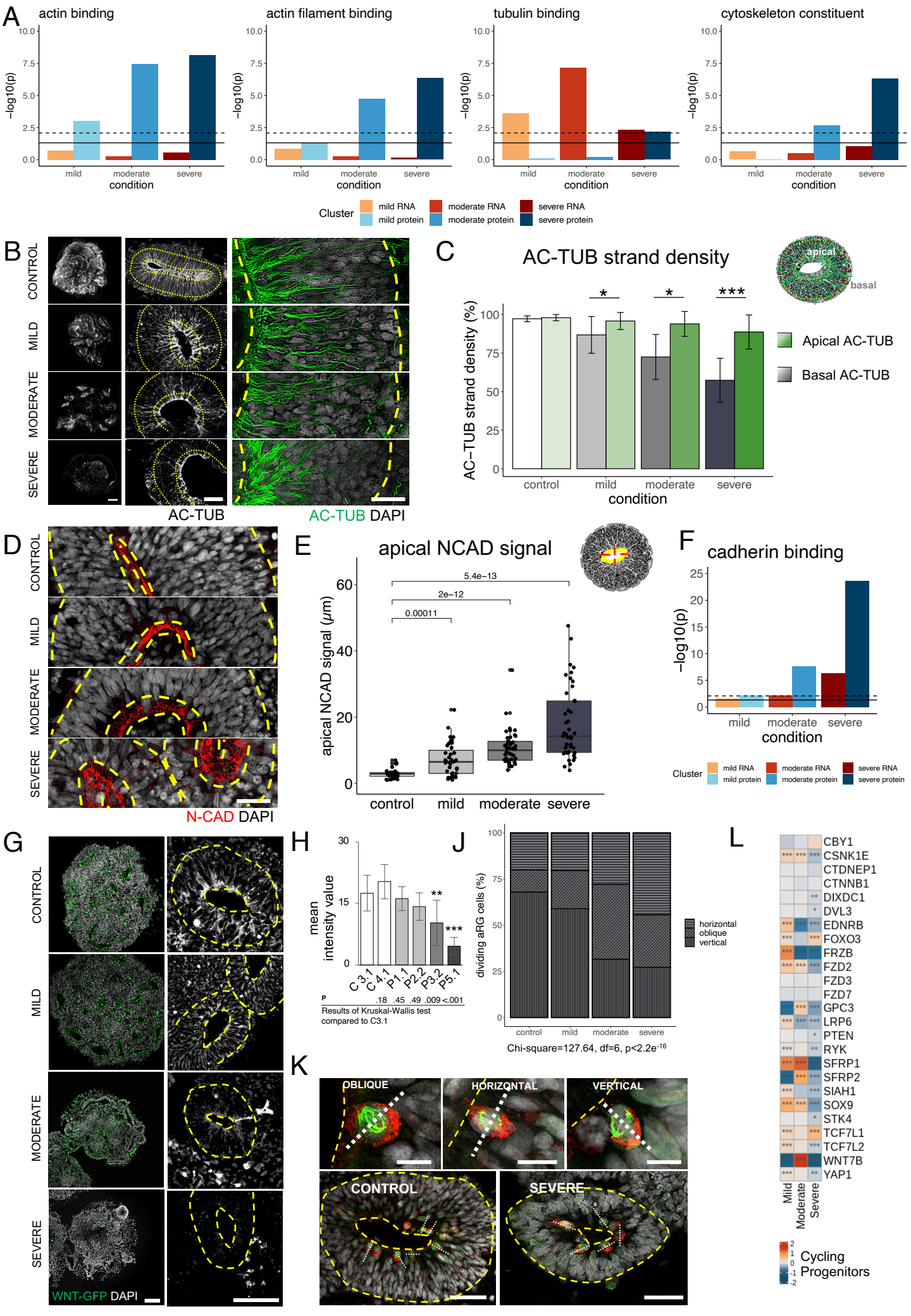
A
actin binding
actin filament binding
tubulin binding
cytoskeleton constituent
−log10(p)
condition
mild
moderate
severe
Cluster
mild RNA
mild protein
moderate RNA
moderate protein
severe RNA
severe protein
B
CONTROL
MILD
MODERATE
SEVERE
AC-TUB
AC-TUB DAPI
C
AC-TUB strand density
AC−TUB strand density (%)
control
mild
moderate
severe
condition
apical
basal
Apical AC-TUB
Basal AC-TUB
D
N-CAD DAPI
E
apical NCAD signal
apical NCAD signal (μm)
5.4e−13
2e−12
0.00011
F
cadherin binding
G
WNT-GFP DAPI
H
mean intensity value
C3.1
C4.1
P1.1
P2.2
P3.2
P5.1
Results of Kruskal-Wallis test compared to C3.1
J
dividing aRG cells (%)
horizontal
oblique
vertical
Chi-square=127.64, df=6, p<2.2e-16
K
OBLIQUE
HORIZONTAL
VERTICAL
CONTROL
SEVERE
L
CBY1
CSNK1E
CTDNEP1
CTNNB1
DIXDC1
DVL3
EDNRB
FOXO3
FRZB
FZD2
FZD3
FZD7
GPC3
LRP6
PTEN
RYK
SFRP1
SFRP2
SIAH1
SOX9
STK4
TCF7L1
TCF7L2
WNT7B
YAP1
Mild
Moderate
Severe
Cycling Progenitors

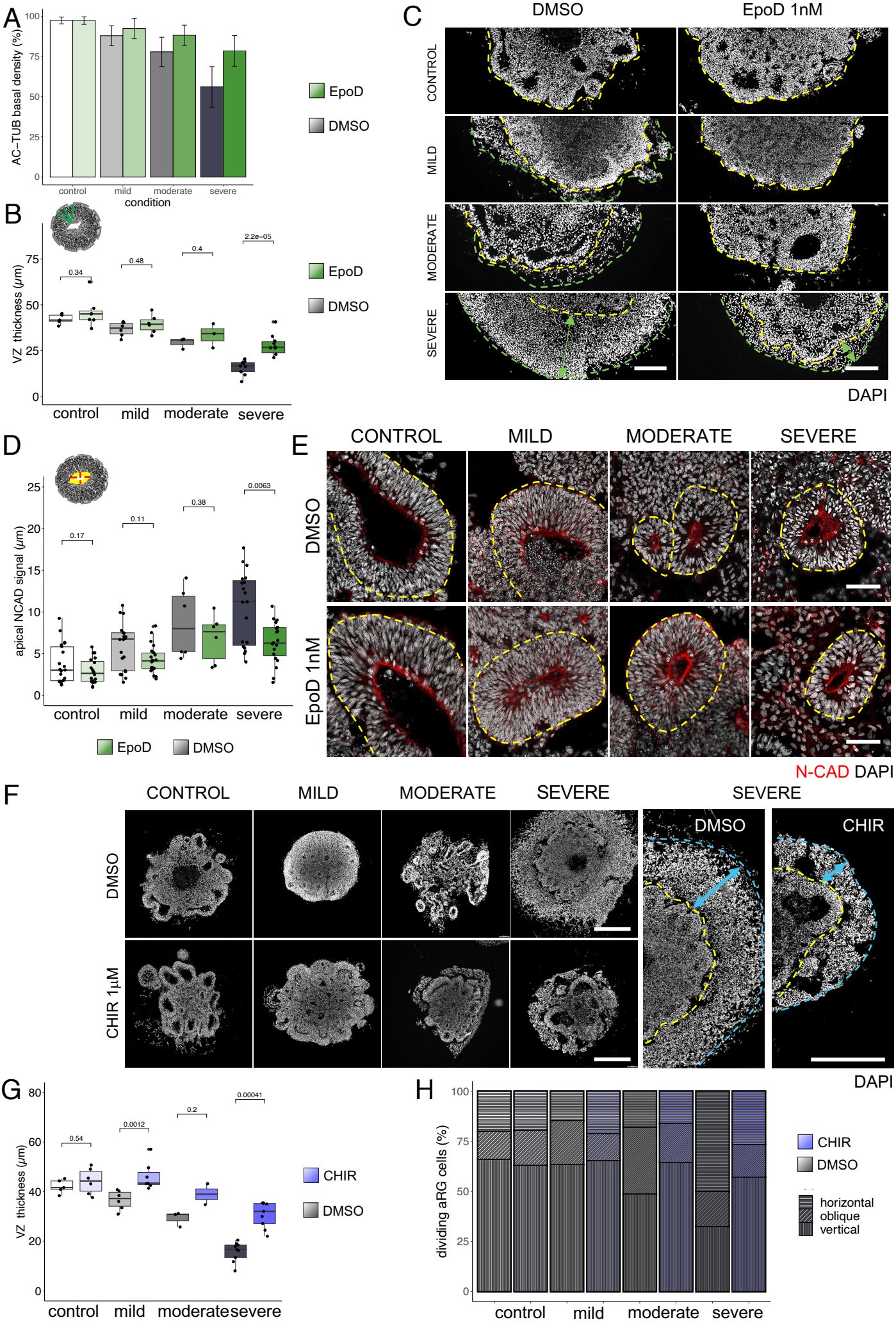
A
AC−TUB basal density (%)
100
75
50
25
0
control
mild
moderate
severe
condition
EpoD
DMSO
B
VZ thickness (μm)
75
50
25
0
0.34
0.48
0.4
2.2e−05
control
mild
moderate
severe
EpoD
DMSO
C
DMSO
EpoD 1nM
CONTROL
MILD
MODERATE
SEVERE
DAPI
D
apical NCAD signal (μm)
25
20
15
10
5
0
0.17
0.11
0.38
0.0063
control
mild
moderate
severe
EpoD
DMSO
E
CONTROL
MILD
MODERATE
SEVERE
DMSO
EpoD 1nM
N-CAD DAPI
F
CONTROL
MILD
MODERATE
SEVERE
SEVERE
DMSO
CHIR
DMSO
CHIR 1μM
DAPI
G
VZ thickness (μm)
80
60
40
20
0
0.54
0.0012
0.2
0.00041
control
mild
moderate
severe
CHIR
DMSO
H
dividing aRG cells (%)
100
75
50
25
0
control
mild
moderate
severe
CHIR
DMSO
horizontal
oblique
vertical